scientific reports

OPEN

Electrospinning preparation of g-C$_3$N$_4$/Nb$_2$O$_5$ nanofibers heterojunction for enhanced photocatalytic degradation of organic pollutants in water

Lu Wang[1,2], Ya Li[3] & Pingfang Han[1]✉

In this study, graphitic carbon nitride (g-C$_3$N$_4$) and niobium pentoxide nanofibers (Nb$_2$O$_5$ NFs) heterojunction was prepared by means of a direct electrospinning approach combined with calcination process. The characterizations confirmed a well-defined morphology of the g-C$_3$N$_4$/Nb$_2$O$_5$ heterojunction in which Nb$_2$O$_5$ NFs were tightly attached onto g-C$_3$N$_4$ nanosheets. Compared to pure g-C$_3$N$_4$ and Nb$_2$O$_5$ NFs, the as-prepared g-C$_3$N$_4$/Nb$_2$O$_5$ heterojunction exhibited remarkably enhanced photocatalytic activity for degradation of rhodamine B and phenol under visible light irradiation. The enhanced catalytic activity was attributed predominantly to the synergistic effect between g-C$_3$N$_4$ sheets and Nb$_2$O$_5$ NFs, which promoted the transferring of carriers and prohibited their recombination, confirmed by the measurement of transient photocurrent responses and photoluminescence spectra. In addition, the active species trapping experiments indicated that superoxide radical anion ($\cdot O_2^-$) and hole (h$^+$) were the major active species contributing to the photocatalytic process. With its high efficacy and ease of preparation, g-C$_3$N$_4$/Nb$_2$O$_5$ heterojunction has great potentials for applications in treatment of organic pollutants and conversion of solar energy.

In recent years, water pollution caused by textile dyes and other organic pollutants has made serious damage to the ecosystem and human health as they are toxic, mutagenic, and mostly non biodegradable[1,2]. For the sustainable development of human being, there is urgent demand to remove water contamination. Traditionally, physical, chemical, and biological wastewater treatment processes are used but generally have several disadvantage such as high cost, low degradation efficiency, etc.[3] Recently, as an ideal "green strategy" to deal with increasing environmental issues, metal oxide semiconductor based photocatalysis has drawn great attention because of their versatile properties[4,5]. In photocatalysis process, when the semiconductors are illuminated by photons with energy higher than their band gap, active charges are generated to cause photocatalytic reactions toward pollutant degradation[6]. Nowadays, semiconductor materials such as TiO$_2$, ZnO, Nb$_2$O$_5$, CeO$_2$, BiOI, graphene, g-C$_3$N$_4$ and their heterojunction composites like Nb$_2$O$_5$/TiO$_2$, BiOI/TiO$_2$, g-C$_3$N$_4$/TiO$_2$, Nb$_2$O$_5$/ZnO and CeO$_2$/Nb$_2$O$_5$ have been used to overcome the water pollution issues[7–20]. Among these semiconductor materials, Nb$_2$O$_5$, a promising traditional semiconductor material with a band gap of ca. 3.2 eV, has been widely used in a variety of fields, for instance, electrode materials, catalysis, photodecomposition of water and especially photodedegradation of harmful organic pollutants in water, due to its outstanding advantages of thermodynamic stability, nontoxicity and relatively high photocatalytic activity[21]. However, the rapid recombination of photogenerated charges hindered the practical application of the pure Nb$_2$O$_5$, similar to other traditional semiconductor photocatalysts[22,23]. With the purpose of facilitating the separation of photoinduced charge, novel Nb$_2$O$_5$-based composites which are suitable for catalysis of pollutant degradation should be constructed. Consequently, researches found that Nb$_2$O$_5$-based heterojunctions with other materials, such as metal (Ag, Au, Pt, etc.), metal oxide (TiO$_2$, NiO, Ag$_2$O, Fe$_2$O$_3$, etc.) and graphene is a prominent method[24–30]. Particularly, Nb$_2$O$_5$ heterojunctions coupled with visible-light-responsive semiconductors are recognized as the most effective photocatalysts for wastewater treatment because of the internal electric field, which can suppress the recombination of photogenerated charge and

[1]College of Biotechnology and Pharmaceutical Engineering, Nanjing Tech University, Nanjing 211816, China. [2]Nantong Vocational University, Nantong 226007, China. [3]Nantong College of Science and Technology, Nantong 226007, China. ✉email: hpf@njtech.edu.cn

effectively improve mutual transfer of photogenerated charge in the heterojunctions, thus ultimately enhance the photocatalytic activity. In addition, visible-light-responsive semiconductor coupling Nb_2O_5 can also improve the light absorption capacity to a significant extent[31].

g-C_3N_4, a two dimensional polymeric semiconductor, has attracted much attention in recently years due to its unique delocalized conjugated π structure formed by sp^2 hybridization of C and N atoms which offers a rapid photoinduced charge separation in the electron transfer process[32]. In particular, g-C_3N_4 can activate molecular oxygen and produce superoxide radicals, which effectively enhances the activities for photocatalytic reactions. Furthermore, g-C_3N_4 shows massive prospects for application of photocatalytic degradation due to its advantages of narrow band gap, low cost, eco-friendliness and excellent optical and thermal properties[33,34]. Unfortunately, the photocatalytic activity of pure g-C_3N_4 is also usually restricted because of the fast recombination of photogenerated electron/hole pairs. In order to improve its efficiency in photocatalytic processes, strategies such as coupling g-C_3N_4 with TiO_2, CeO_2, $BiVO_4$ have been proposed, which can not only effectively reduce the photoinduced electron–hole recombination rate, but also form intermediate energy levels in the forbidden band of metal oxide owing to the matching band structure of g-C_3N_4 and metal oxide[35–37]. So far, many g-C_3N_4/Nb_2O_5 heterojunction photocatalysts have been successfully prepared to enhance photocatalytic activity for pollutants degradation due to the well match of band gap edges between Nb_2O_5 and g-C_3N_4, which facilitates the charge carrier separation and thus improves the photocatalytic performance. Carvalho et al. reported that g-C_3N_4/Nb_2O_5 heterojunction photocatalysts, assembled as Nb_2O_5 nanoparticles decorating the g-C_3N_4 surface via hydrothermal process, exhibited remarkable enhanced photocatalytic activity in the degradation of methylene blue and rhodamine B dyes[38]. Silva et al. reported that g-C_3N_4/Nb_2O_5 heterostructures, assembled as Nb_2O_5 nanospheres decorating the g-C_3N_4 surface by a sonochemical method, showed high activity for dye and drug pollutants degradation under visible light irradiation[39]. Hong et al. reported Nb_2O_5/g-C_3N_4 heterojunctions prepared by a simple heating method showed significantly enhanced photocatalytic activity in the degradation of tetracycline hydrochloride[40]. As shown in these reports, the g-C_3N_4/Nb_2O_5 heterojunction had excellent photocatalytic performance and remarkable optoelectronic characteristics for degrading organic pollutants in wastewater compared with individual g-C_3N_4 and pure Nb_2O_5. Nevertheless, most of these studies were based on powder-form Nb_2O_5, which was prepared by complicated means such as solvothermal method, chemical precipitation method, et al. These conventional preparation methods may lead to agglomeration of Nb_2O_5 nanoparticles and then reduce the photocatalytic activity. Hence, it is of great interest to develop a facile and practical method for effective preparation of the evenly nanostructured g-C_3N_4/Nb_2O_5 heterojunction with large specific surface area and improved photocatalytic activity.

To date, one-dimensional semiconductor metal oxide nanofibers fabricated through electrospinning have been greatly attractive due to the advantages of high surface areas and large surface-to-volume ratio, which can provide quick charge transfer channels and more active sites[41–44]. More significantly, the electrospun nanofibers with a rather high surface area will be optimal carriers for fabricating heterojunction photocatalysts and then provide more active reaction sites for interaction with pollutants[45]. Meanwhile, the electrospun nanofibers with nonwoven web structure results in an easy separation and recovery from fluid in photocatalytic process[46,47]. On the basis of above, constructing heterojunctions of electrospun Nb_2O_5 nanofibers coupled with g-C_3N_4 would be expected as promising composite photocatalyst for practical applications.

In the present work, we developed a g-C_3N_4/Nb_2O_5 nanofibers heterojunction via a simple electrospinning technique, which exhibited a photocatalytic activity superior to the pure g-C_3N_4 and electrospun Nb_2O_5 NFs. Meanwhile, the as-prepared heterojunction could be recovered easily by filtration without reducing the photocatalytic activity. Moreover, a possible degradation mechanism is also proposed based on the detailed structural analysis of the heterojunction.

Experimental

Synthesis of g-C_3N_4/Nb_2O_5 heterojunction.   In a typical procedure, g-C_3N_4/Nb_2O_5 heterojunction was synthesized by electrospinning. First, 10 g of CH_6ClN_3 was heated in an open crucible in static air at a heating rate of 10 °C/min to 600 °C and kept at that temperature for 4 h. The product was collected and ground into powder in an agate mortar to obtain the g-C_3N_4. Subsequently, 0.25 g of $NbCl_5$ and 0.025 g of g-C_3N_4 were added into 2.65 mL of N,N-dimethylformamide (DMF) and ultrasonicated for 1 h. Then 0.35 g of polyvinylpyrrolidone (PVP) was dissolved in the mixture. After magnetic stirring for 8 h, the precursor solution of g-C_3N_4/$NbCl_5$/PVP composite was afforded and transferred into a 5 mL plastic syringe with a 25 gauge stainless steel needle for electrospinning. In this electrospinning experiment, the collector was positioned 20 cm away from the tip of needle and the applied direct voltage between the collector and the needle tip was ~ 18 kV, the precursor solution flow rate was 0.25 mL/h. Then, the collected precursor nanofibers were calcined in muffle furnace at 600 °C for 1 h in air with a heating rate of 10 °C/min to obtain g-C_3N_4/Nb_2O_5 heterojunction. For comparison, pure Nb_2O_5 nanofibers was prepared under the same condition without adding g-C_3N_4.

Characterizations and photocatalytic experiment.   Supporting Materials showed their details.

Results and discussion

Characterization.   The Fourier Transform infrared (FTIR) spectra of as prepared samples were shown in Fig. 1. In the FTIR spectrum of Nb_2O_5 NFs, the peaks at 827 cm^{-1} and 665 cm^{-1} were assigned to Nb–O–Nb and Nb=O bonds of Nb_2O_5, respectively[48]. For g-C_3N_4, the broad adsorption band centered at 3188 cm^{-1} and the peak at 1637 cm^{-1} belong to the stretching vibration mode of terminal NH groups and the C=N stretching vibration modes, respectively. The peaks around at 1411 cm^{-1}, 1317 cm^{-1} and 1238 cm^{-1} were attributed to aromatic C–N stretching. The unique absorption peak at approximately 806 cm^{-1} was related to the s-triazine ring
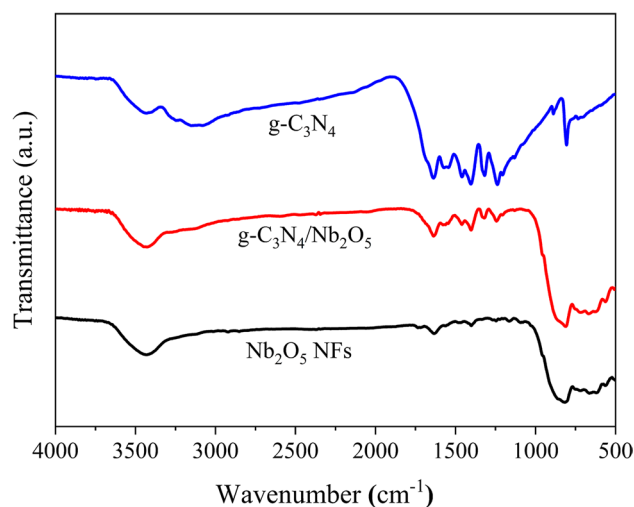
**Figure 1.** FTIR spectrum of g-C_3N_4, Nb_2O_5 NFs and g-C_3N_4/Nb_2O_5 heterojunction.
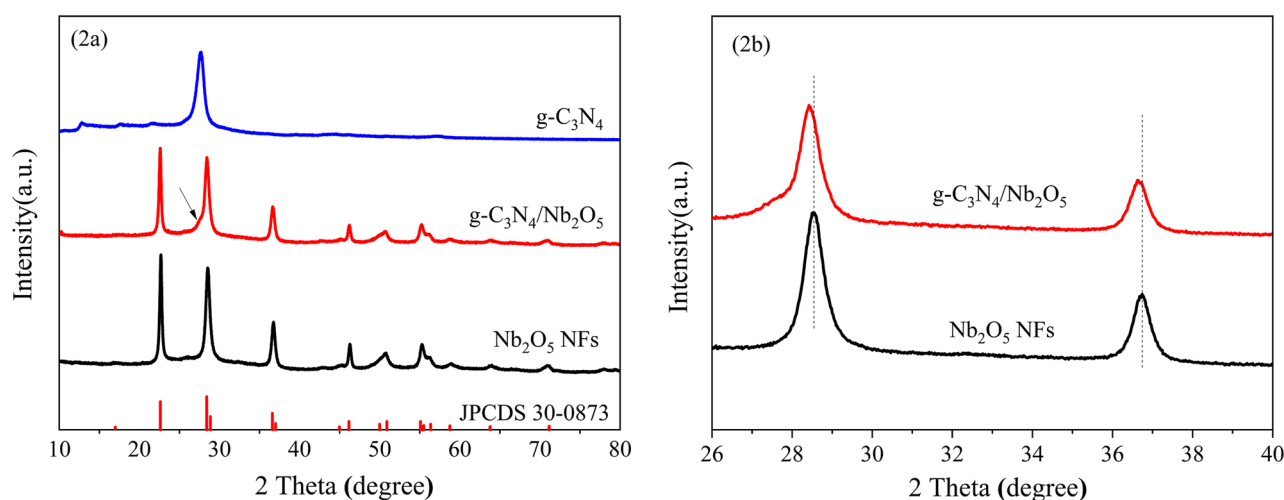
Figure 2. (**a**) XRD patterns of g-C_3N_4, Nb_2O_5 NFs and g-C_3N_4/Nb_2O_5 heterojunction and (**b**) enlarge of 2 theta scale at 26°–40° region of Nb_2O_5 NFs and g-C_3N_4/Nb_2O_5 heterojunction.

modes[49]. As expected, all of the major characteristic absorption peaks of g-C_3N_4 and Nb_2O_5 were present in the spectrum of g-C_3N_4/Nb_2O_5 heterojunction, suggesting that composite samples contained g-C_3N_4.

Figure 2 depicted the X-ray diffraction (XRD) patterns of g-C_3N_4, Nb_2O_5 NFs and g-C_3N_4/Nb_2O_5 heterojunction. As shown in Fig. 2a, the quintessential characteristic diffraction peaks of pure g-C_3N_4 at 13.4° and 27.6° associated to the (100) and (002) planes of the graphite-like structure of C_3N_4, respectively[50]. The XRD pattern revealed that the diffraction peaks of Nb_2O_5 NFs correspond to the orthorhombic phase (standard JCPDS card 30-0873). It is noticeable that the synthesized g-C_3N_4/Nb_2O_5 heterojunction exhibited similar pattern to Nb_2O_5 NFs. The characteristic peak of g-C_3N_4 (002) closed to orthorhombic (180) peak was not extrusive in the pattern of g-C_3N_4/Nb_2O_5 heterojunction owing to the comparatively low dosage of g-C_3N_4. Moreover, compared with Nb_2O_5 NFs, the diffraction peaks of Nb_2O_5 in the heterojunction became weaker and shifted slightly to a smaller value diffraction angle (Fig. 2b) with the addition of g-C_3N_4, which may be caused by the interaction between g-C_3N_4 and Nb_2O_5 in the heterojunction. Similar phenomenon was also reported in an earlier literature[51].

Fig. S1 showed the thermogravimetric analysis (TGA) curves of g-C_3N_4 and g-C_3N_4/Nb_2O_5 heterojunction. The thermal profile of g-C_3N_4 indicated that the as-prepared material was stable in air flow below 600 °C, and heating to 700 °C resulted in no residue of the material being observable[52]. The weight of the g-C_3N_4/Nb_2O_5 heterojunction decreased rapidly in the temperature range 600–700 °C, owing to the demoposition of g-C_3N_4 occurred in this temperature range. Hence, the g-C_3N_4 content for the g-C_3N_4/Nb_2O_5 heterostructure could be estimated to be 9.2 wt% neglecting the amount of surface-bound water.

The morphology of g-C_3N_4, Nb_2O_5 NFs and g-C_3N_4/Nb_2O_5 heterojunction were observed by scanning electron microscopy (SEM) and transmission electron microscope (TEM). It was found that the Nb_2O_5 NFs represent 1D nanofiber morphology, which had an average diameter of 150 nm with random orientation (Fig. S2a). The
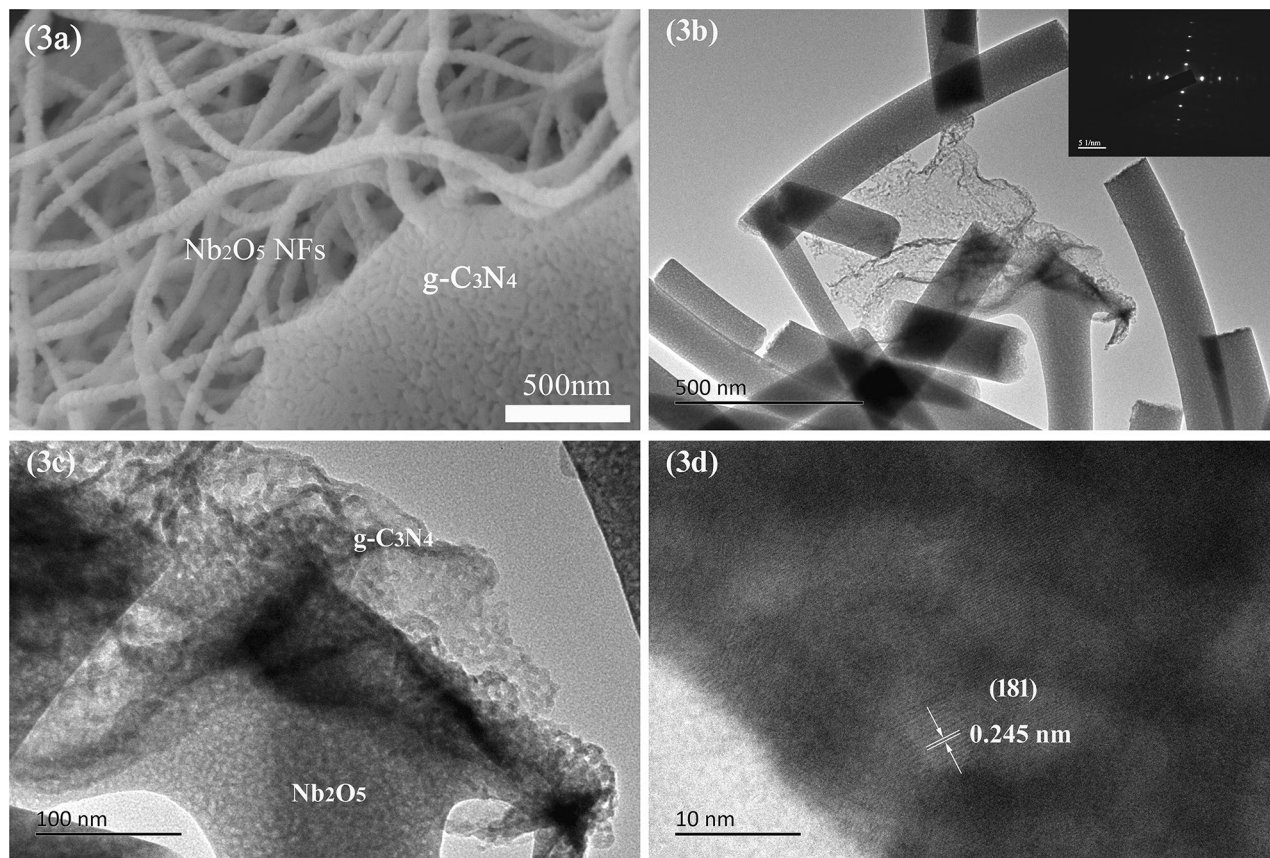
Figure 3. (**a**) SEM, (**b**,**c**) TEM and (**d**) high resolution TEM images of g-C$_3$N$_4$/Nb$_2$O$_5$ heterojunction. The inset of (**b**) is SAED pattern of g-C$_3$N$_4$/Nb$_2$O$_5$ heterojunction.

g-C$_3$N$_4$ sample displayed an irregular sheet like structure (Fig. S2b). It was perceptible on the SEM image of g-C$_3$N$_4$/Nb$_2$O$_5$ heterojunction (Fig. 3a) that two semiconductors, Nb$_2$O$_5$ nanofibers and g-C$_3$N$_4$, directly and sufficiently contacted through mixed eletrospinning process and calcination. Such line/area contact increased porosity-related characteristics of the heterojunction and resulted in less agglomeration. In particular, such heterojunction formed by nanofiber and nanosheet can enhance the transport of charges and reduce the recombination probability of photoexcited charge carriers, ultimately further improve the photodegradation efficiency[53]. TEM image (Fig. 3b) further revealed that the g-C$_3$N$_4$/Nb$_2$O$_5$ heterojunction was composed of homogeneous, long and narrow Nb$_2$O$_5$ NFs that were in direct contact with g-C$_3$N$_4$ nanosheets. In addition, the selected area electron diffraction (SAED) pattern (inset of Fig. 3b) depicted broad and strong spots that was assigned to the essentially 1D characteristic of the long nanofibers, indicating the highly single crystallinity of the orthorhombic-phase Nb$_2$O$_5$[54,55], which was in accordance with the XRD analysis results of Nb$_2$O$_5$. No diffraction spots/rings of g-C$_3$N$_4$ were detected in the SAED spectrum, indicating that g-C$_3$N$_4$ was amorphous in the g-C$_3$N$_4$/Nb$_2$O$_5$ heterojunction[56]. Figure 3c exhibited that Nb$_2$O$_5$ NFs with a distribution of diameters ~ 150 nm were attached onto the surfaces of g-C$_3$N$_4$ nanosheets, forming g-C$_3$N$_4$/Nb$_2$O$_5$ heterojunction structure. Moreover, the high resolution TEM image (Fig. 3d) revealed the lattice fringe with d-spacing of approximately 0.245 nm, which was in agreement with the (181) spacing of orthorhombic Nb$_2$O$_5$[57]. With these, a heterojunction formation between Nb$_2$O$_5$ and g-C$_3$N$_4$ was confirmed. This heterojunction would promote charge transfer between Nb$_2$O$_5$ and g-C$_3$N$_4$ and separation of photogenerated electron–hole pairs, both of which would enhance the photocatalytic activity.

The X-ray photoelectron spectroscopy (XPS) survey spectrum and high resolution spectrum of g-C$_3$N$_4$/Nb$_2$O$_5$ heterojunction were performed to illuminate the surface composition and the chemical environment. As shown in Fig. 4a, the survey XPS spectrum exhibited that the g-C$_3$N$_4$/Nb$_2$O$_5$ heterojunction not only contained Nb, O elements related to the Nb$_2$O$_5$ phase, but also contained C, N elements related to the g-C$_3$N$_4$ phase. Correspondingly, the C 1 s high-resolution spectra (Fig. 4b) was divided into three fitted peaks at 284.78 eV, 286.28 eV and 288.43 eV. The peak at 284.78 eV corresponded to sp^2-hybridized carbon atoms of the carbon standard used to calibrate the binding energies. The peaks at 286.28 eV and 288.43 eV was attributed to the C–N–C and N–C=N backbones coordination in the triazine rings of g-C$_3$N$_4$, respectively[58]. The N 1s high-resolution spectra (Fig. 4c) was deconvoluted into two fitted peaks at 398.93 eV and 401.13 eV, which could be assigned to N sp^2-bonded to C (N-sp^{2}C) and tertiary nitrogen groups (N-(C)$_3$) of g-C$_3$N$_4$, respectively[59]. The Nb 3d spectrum (Fig. 4d) exhibited two significant peaks at around 207.43 and 210.13 eV, corresponding to 3d$_{5/2}$ and 3d$_{3/2}$ states of Nb^{5+}, respectively[60]. The O 1s XPS spectrum (Fig. 4e) could be fitted to two peaks centered at around 530.28 and
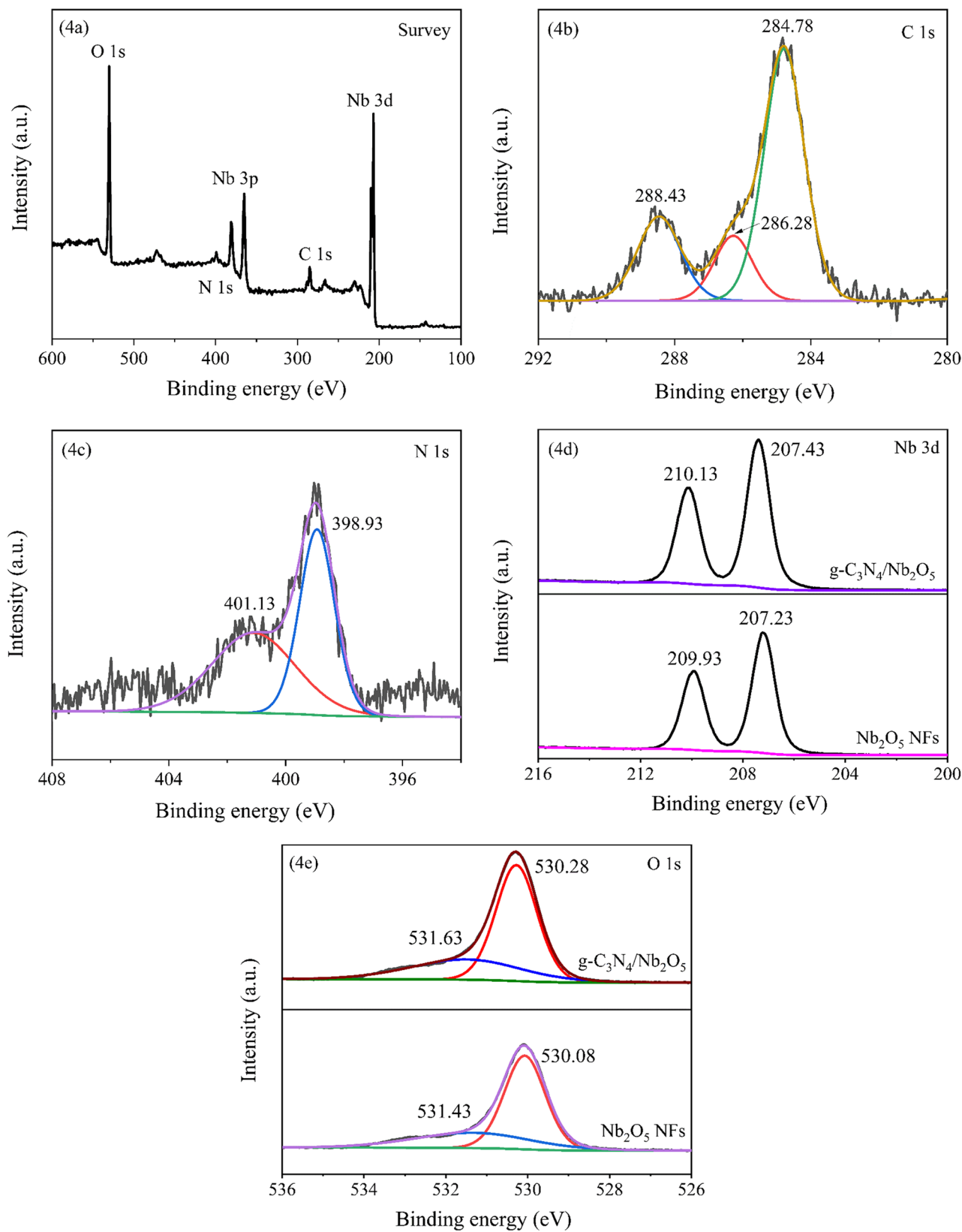
Figure 4. (**a**) XPS survey spectrum and high resolution XPS spectra of (**b**) C 1s, (**c**) N 1s, (**d**) Nb 3d and (**e**) O 1s in g-C_3N_4/Nb_2O_5 heterojunction.
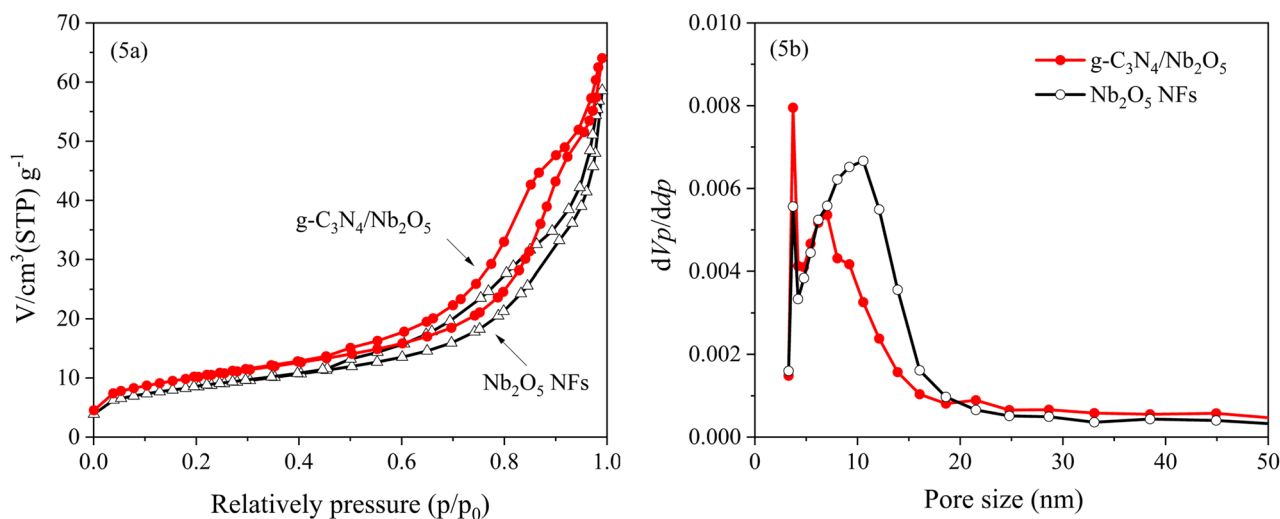
Figure 5. (**a**) N_2 sorption isotherm and (**b**) pore size distribution of Nb_2O_5 NFs and g-C_3N_4/Nb_2O_5 heterojunction.
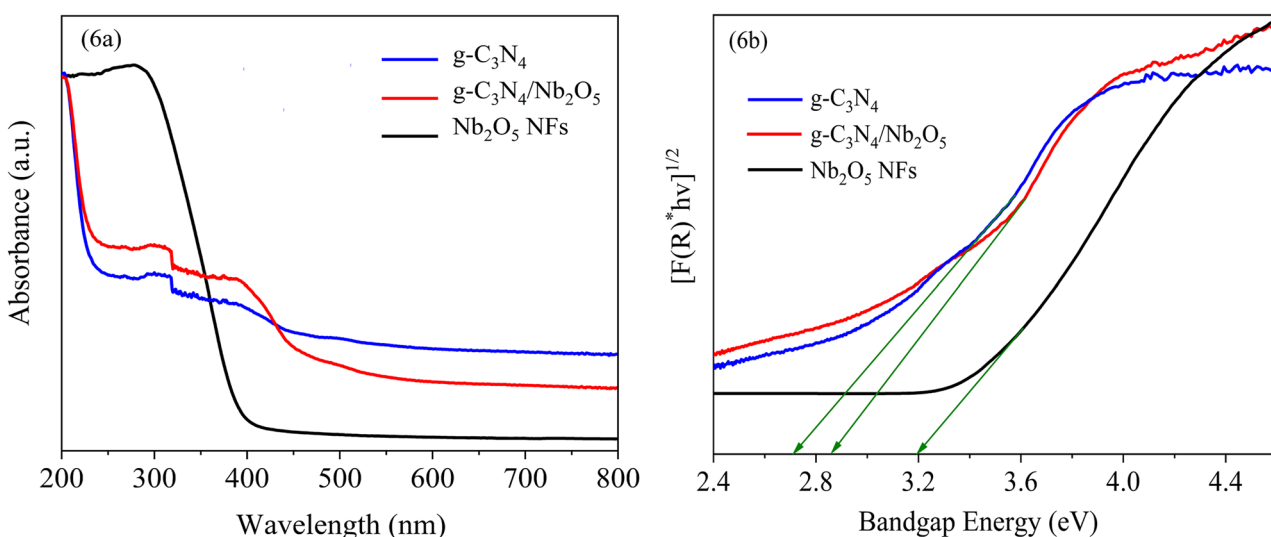
Figure 6. (**a**) UV–vis diffused reflectance spectra and (**b**) Tauc plot graph of g-C_3N_4, Nb_2O_5 NFs and g-C_3N_4/Nb_2O_5 heterojunction.

531.63 eV, which were assigned to the Nb–O bond and adsorbed oxygen, respectively. Notably, compared with those of pure Nb_2O_5 NFs, the Nb 3d and O 1s peaks of g-C_3N_4/Nb_2O_5 heterojunction shifted slightly to higher energies, evidencing the intense interaction between the Nb_2O_5 and g-C_3N_4 that resulted from the formation of effective heterojunction. These phenomena are in good agreement with previous report[53].

Figure 5 showed N_2 absorption–desorption isotherms and pore size distribution curves of Nb_2O_5 NFs and g-C_3N_4/Nb_2O_5 heterojunction. As illustrated in Fig. 5a, both the isotherms belonged to type IV isotherm possessed obvious type H_3 hysteresis loop at relative higher p/p_0, suggesting the existence of slit-shaped pores due to the aggregation of nanoparticles[61]. The BET specific surface areas of Nb_2O_5 NFs and g-C_3N_4/Nb_2O_5 heterojunction are 30.09 m^2/g and 36.18 m^2/g, respectively. In addition, Fig. 5b displays the pore-size distributions of Nb_2O_5 NFs and g-C_3N_4/Nb_2O_5 heterojunction estimated with the BJH method. As seen from the spectra, two characteristic diameters of mesopores (2–50 nm) are located primarily at 3.7 and 10.6 nm for pure Nb_2O_5 NFs, 3.7 and 7.1 nm for g-C_3N_4/Nb_2O_5 heterojunction, respectively. The increased BET specific surface area and decreased pore size were likely caused by the incorporation of g-C_3N_4, which was fundamental in enhancing the photodegradation activity of electrospun g-C_3N_4/Nb_2O_5 heterojunction.

The UV–Vis absorption spectra of as-prepared samples were depicted in Fig. 6a. It is obvious that the g-C_3N_4 has absorption in the visible region, which is in good agreement with the narrow band gap. However, the Nb_2O_5 NFs only absorbs UV light, consistent with wide band gap. Compared to Nb_2O_5 NFs, the absorption edge of g-C_3N_4/Nb_2O_5 heterojunction shifts to the visible light region with the absorbance edge between those of Nb_2O_5 NFs and g-C_3N_4. It can be concluded that the combination of g-C_3N_4 and Nb_2O_5 may enhance the visible light absorption of the sample and thus improve their catalytic activity in the visible region[35]. In addition, the bandgap
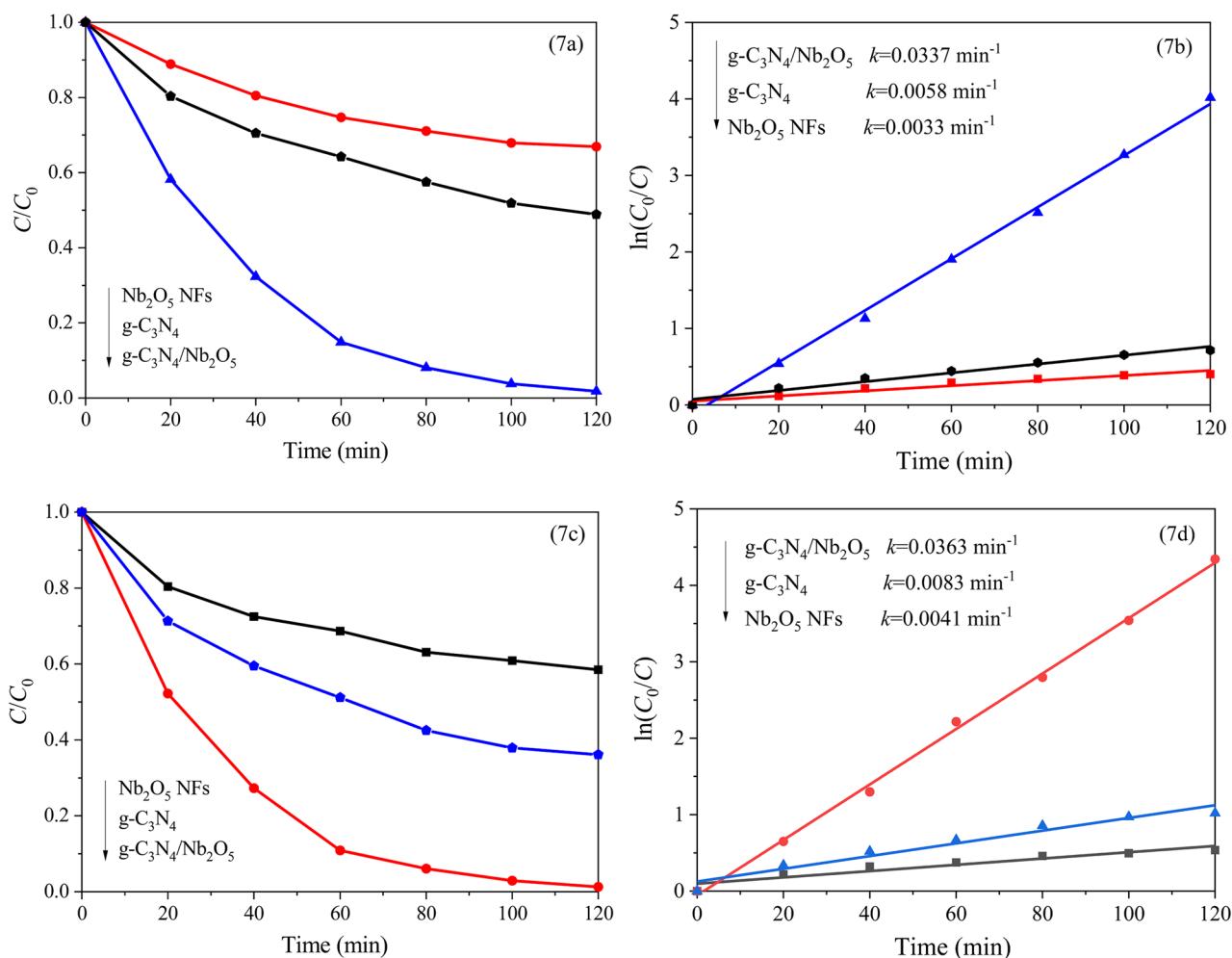
Figure 7. The degradation efficiency of (**a**) RhB and (**b**) phenol, kinetics curves for (**c**) RhB and (**d**) phenol over g-C₃N₄, Nb₂O₅ NFs and g-C₃N₄/Nb₂O₅ heterojunction under visible light irradiation.

energy of samples were obtained from Tauc plot by extrapolation to the photon energy-axis. As illustrated in Fig. 6b, the band gap values of the g-C$_3$N$_4$ and Nb$_2$O$_5$ NFs were estimated to be approximately 2.7 and 3.2 eV, respectively, consistent with those described for these phases in the literature[31,62]. In addition, the band gap of g-C$_3$N$_4$/Nb$_2$O$_5$ heterojunction was found to be 2.84 eV. This suggested that the synthetized g-C$_3$N$_4$/Nb$_2$O$_5$ heterojunction had smaller band gap than that of pure Nb$_2$O$_5$ NFs, which was the precondition of effective photocatalytic activity in visible region. Besides, Mott–Schottky plots (Fig. S3) of the Nb$_2$O$_5$ NFs and g-C$_3$N$_4$ were collected to define their conduction band potential (E_{CB}). The derived E_{CB} of Nb$_2$O$_5$ NFs and g-C$_3$N$_4$ were estimated to be – 0.59 and – 0.98 eV, respectively[63]. Thus, the valence band potential (E_{VB}) of them were calculated to be 2.61 and 1.72 eV, respectively.

Photocatalysis. The photocatalytic activities of the synthetized samples were investigated by decomposing rhodamine B (RhB) under visible light irradiation. As shown in Fig. 7a, compared to Nb$_2$O$_5$ NFs and g-C$_3$N$_4$, g-C$_3$N$_4$/Nb$_2$O$_5$ heterojunction possessed the highest photocatalytic degradation rate owing to the existence of synergistic effect between g-C$_3$N$_4$ and Nb$_2$O$_5$. After 120 min irradiation, the photodegradation efficiency of RhB for g-C$_3$N$_4$/Nb$_2$O$_5$ heterojunction was 98.1%. The superior photocatalytic activity of g-C$_3$N$_4$/Nb$_2$O$_5$ heterojunction over RhB could also be confirmed from kinetics experiment. On the base of the rate equation of $-\ln(C/C_0) = kt$, k representing the degradation rate constant, the kinetic curves for the RhB photodegradation over three photocatalysts were obtained, as shown in Fig. 7b. It was obviously that the k value of g-C$_3$N$_4$/Nb$_2$O$_5$ heterojunction is larger than that of Nb$_2$O$_5$ NFs and g-C$_3$N$_4$. In addition, phenol, a colorless organic pollutant model, was selected to further evaluate the photocatalytic activity of g-C$_3$N$_4$/Nb$_2$O$_5$ heterojunction. It can be found that the g-C$_3$N$_4$/Nb$_2$O$_5$ heterojunction also displayed the highest photocatalytic activity for phenol degradation. It was observed that essentially complete degradation of phenol occured over 120 min for g-C$_3$N$_4$/Nb$_2$O$_5$ heterojunction (Fig. 7c). The degradation rate constant of phenol over different catalysts were also calculated by the above rate equation. It is found that g-C$_3$N$_4$/Nb$_2$O$_5$ heterojunction still achieved the highest apparent rate constant among all these samples (Fig. 7d). Meanwhile, the total organic carbon (TOC) removal rate of g-C$_3$N$_4$/Nb$_2$O$_5$ heterojunction sample for degradation of RhB and phenol were shown in Fig. S4. It can be seen that

Preparation method	Morphology of Nb_2O_5	Organic pollutants	Initial concentration (mg L^{-1})	Removal (%)	Conditions	Ref
Calcination	Nanoparticles	Tetracycline hydrochloride	20	76.2	Visible light, 150 min	[40]
				90.1	Simulated solar light, 60 min	
Sonochemical method	Nanoparticles	Amiloride	10	89	Visible light, 180 min	[39]
		Rhodamine B	10	81	Visible light, 90 min	
Thermal oxidation and hydrothermal treatment	Nanoparticles	Methylene blue	10	82	UV light, 210 min	[38]
			10	65	Visible light, 210 min	
Electrospinning	Nanofibers	Rhodamine B	10	98.1	Visible light, 120 min	Present work
		Phenol	10	98.7	Visible light, 120 min	

**Table 1.** Summary of the photocatalytic activity on various $g-C_3N_4/Nb_2O_5$ composites.
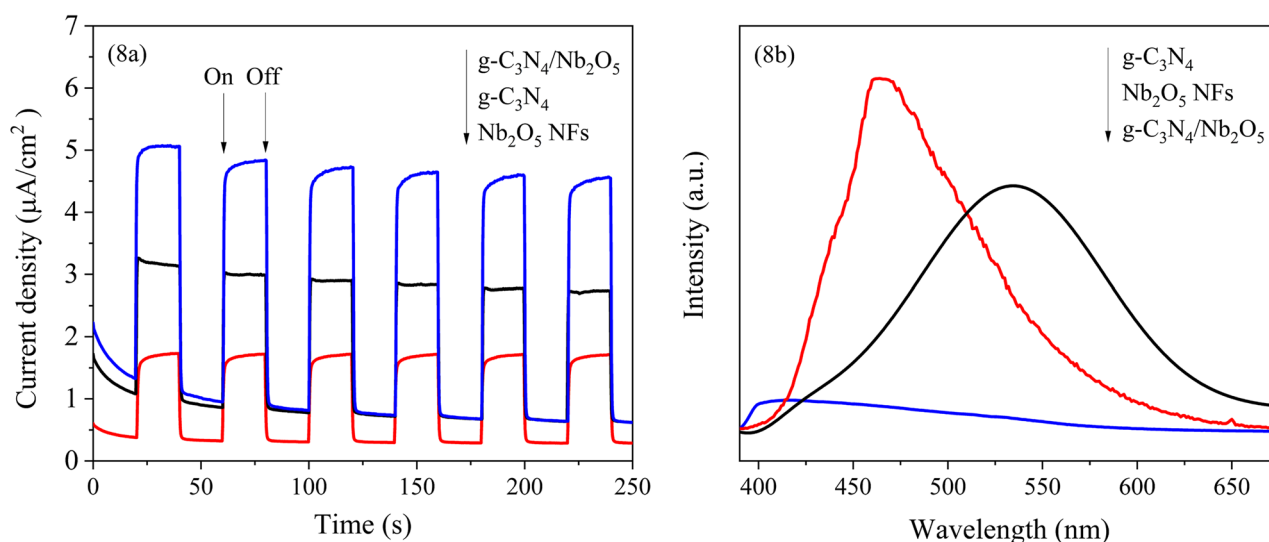
Figure 8. (**a**) Transient photocurrent response and (**b**) PL spectra of $g-C_3N_4$, Nb_2O_5 NFs and $g-C_3N_4/Nb_2O_5$ heterojunction.

the TOC of both solutions decreased as the reaction time increased and reached almost to zero indicating that mineralization of the pollutants occur during the photocatalytic reaction[64]. Table 1 presented the photocatalytic degradation rate of various $g-C_3N_4/Nb_2O_5$ composites, which are comparable to as-synthesized $g-C_3N_4/Nb_2O_5$ heterojunction, is exhibited remarkable degradation rate.

Photocatalysis mechanism. Investigating the lifetime of photoexcited charge carriers is fundamental to understand the photocatalysis mechanism. The photocurrent responses of $g-C_3N_4$, Nb_2O_5 NFs and $g-C_3N_4/Nb_2O_5$ heterojunction were undertaken to manifest the separation efficiency of the electron–hole pairs. As shown in Fig. 8a, $g-C_3N_4/Nb_2O_5$ heterojunction exhibited the strongest photocurrent density in comparison with that of the single component, which reflected the reduced interface resistance and the enhanced separation and migration efficiency of the photoinduced electron–hole pairs in $g-C_3N_4/Nb_2O_5$ heterojunction[65]. This was also consistent with the photoluminescence (PL) spectroscopy results. Based on Fig. 8b, it can be seen that the peak intensities gradually decrease in the order of $g-C_3N_4$, Nb_2O_5 NFs and $g-C_3N_4/Nb_2O_5$ heterojunction, indicating the $g-C_3N_4/Nb_2O_5$ heterojunction possessing the lowest electron–hole recombination efficiency. It can be concluded that the recombination of photogenerated charge carriers were inhibited effectively due to the heterojunction construction of $g-C_3N_4$ and Nb_2O_5[66].

On the other side, hydroxyl radical (·OH), hole (h⁺) and superoxide radical anion (·O_2^-) as major active species play key roles in photocatalytic reaction. To elucidate the mechanism of $g-C_3N_4/Nb_2O_5$ heterojunction, free radicals trapping experiments were performed to confirm the active species contributing to RhB and phenol photodegradation. In these experiments, isopropanol (IPA), triethanolamine (TEA) and p-benzoquinone (BZQ) acted as the scavenger for ·OH, h⁺ and ·O_2^-, respectively. Figure 9 revealed the photocatalytic efficiencies of RhB and phenol with $g-C_3N_4/Nb_2O_5$ heterojunction after adding various scavengers. The reaction rate constant showed almost unchanged in the presence of IPA, while the addition of TEA and BZQ led to an obviously decrease of the reaction rate constant. In view of the above results, it can be proposed that ·O_2^- is the main active species and h⁺ also play important role in $g-C_3N_4/Nb_2O_5$ heterojunction for RhB and phenol degradation.

Based on the above analysis and experiments, the mechanism was proposed and schematically illustrated in the Fig. 10. It was well understood that the distinction of CB edge potentials between semiconductors strongly
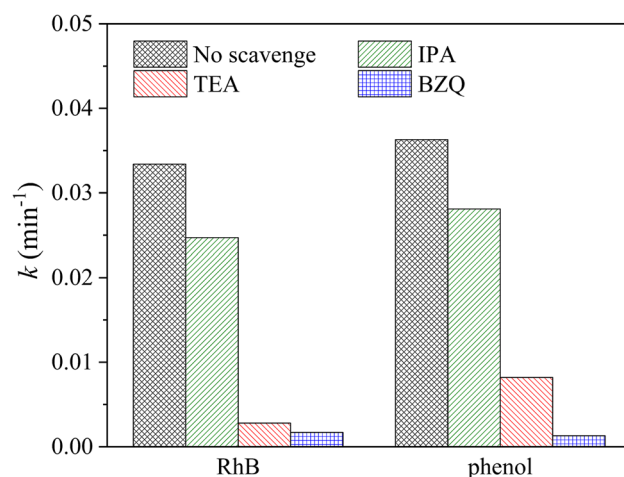
Figure 9. Effects of different scavengers on RhB and phenol photodegradation over the g-C$_3$N$_4$/Nb$_2$O$_5$ heterojunction.
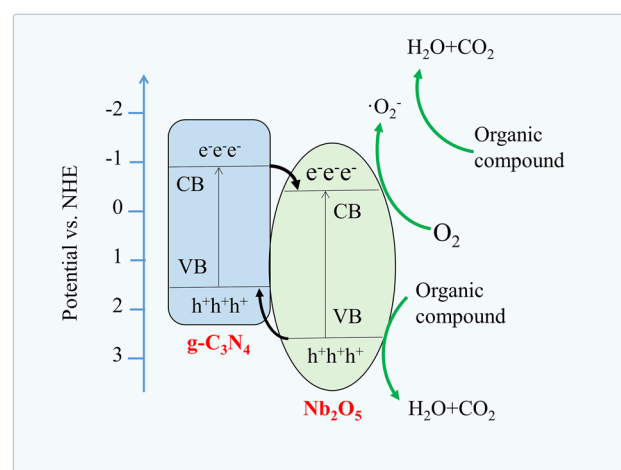
Figure 10. Schematic diagram of photogenerated charges in g-C$_3$N$_4$/Nb$_2$O$_5$ heterojunction.

promoted the electrons transfer at the heterojunction interface and reduced the recombination of carriers, ultimately improved the photodegradation activity of heterojunction[67]. When g-C$_3$N$_4$/Nb$_2$O$_5$ heterojunction was exposed to irradiation, g-C$_3$N$_4$ component was easy to be excited by visible light due to its narrow band gap. And the photogenerated electrons were easy to transfer from CB of g-C$_3$N$_4$ to that of Nb$_2$O$_5$ because the CB edge potential of g-C$_3$N$_4$ (− 0.98 eV) was more negative than that of Nb$_2$O$_5$ (− 0.59 eV). The photogenerated electrons could react with dissolved O$_2$ near the Nb$_2$O$_5$ NFs to form the main active specie of ·O$_2^-$, which was mostly responsible for degrading pollutants. Similarly, the VB edge potential of g-C$_3$N$_4$ (1.72 eV) was also more negative than that of Nb$_2$O$_5$ (2.61 eV), and the photogenerated h$^+$ transfer to VB of g-C$_3$N$_4$ from VB of Nb$_2$O$_5$ through the tight heterojunction interface. The residual h$^+$ on VB of Nb$_2$O$_5$ could oxidize organic molecules to photodegradation products directly. Moreover, the multi-point connected Nb$_2$O$_5$ nanofiber and porous g-C$_3$N$_4$ were also helpful to promote the electron migration.

Reusability of g-C$_3$N$_4$/Nb$_2$O$_5$ heterojunction. To investigate the stability and reusability of the g-C$_3$N$_4$/Nb$_2$O$_5$ heterojunction, recycling test of the photodegradation were performed. After each photodegradation cycle, the catalyst was filtered from the solution and dried at 80 °C for further use. As depicted in Fig. 11a, the g-C$_3$N$_4$/Nb$_2$O$_5$ heterojunction showed no obvious reduction of photocatalytic activity after four cycles for both RhB and phenol, demonstrating its excellent stability and reusability for the multiple times for organic pollutants degradation. And the XRD patterns of the g-C$_3$N$_4$/Nb$_2$O$_5$ heterojunction before and after the reaction were similar (Fig. 11b). From a typical SEM image of g-C$_3$N$_4$/Nb$_2$O$_5$ heterojunction (inset of Fig. 11b) after photocatalytic reaction, it can be clearly seen that the Nb$_2$O$_5$ NFs is still tightly attached with g-C$_3$N$_4$ nanosheet, which indicates that the morphology of g-C$_3$N$_4$/Nb$_2$O$_5$ heterojunction remains unchanged after photocatalytic reaction.
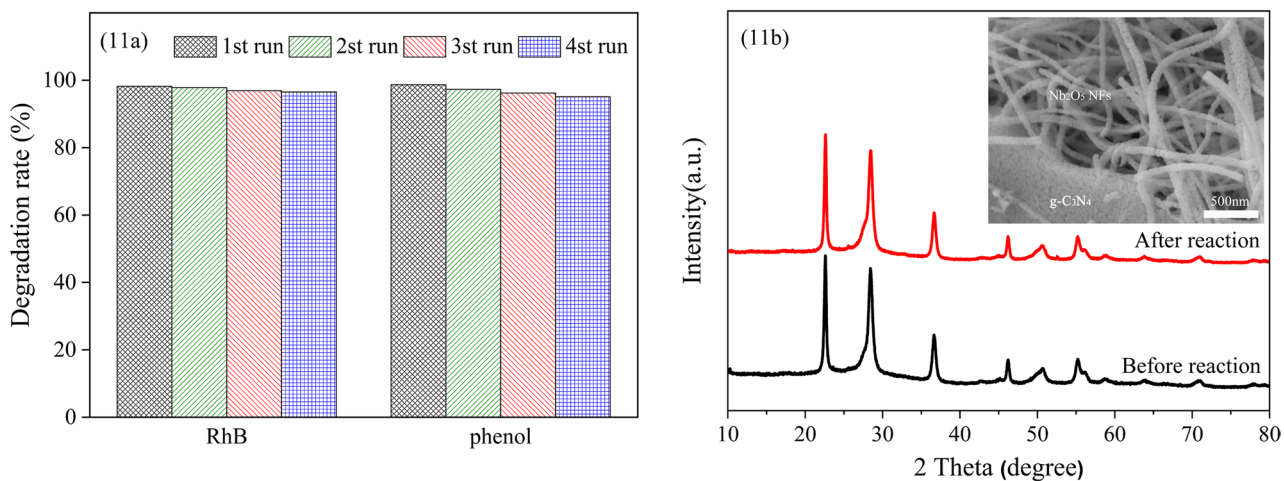
Figure 11. (**a**) The reusability of g-C$_3$N$_4$/Nb$_2$O$_5$ heterojunction: photodegradation of RhB and phenol. (**b**) XRD patterns of g-C$_3$N$_4$/Nb$_2$O$_5$ heterojunction before and after photodegradation, and a typical SEM image (inset) of g-C$_3$N$_4$/Nb$_2$O$_5$ heterojunction after the photodegradation.

Conclusions

In summary, the g-C$_3$N$_4$/Nb$_2$O$_5$ heterojunction was successfully synthesized using a simple and facile electro-spinning-calcination process and displayed excellent photocatalytic activity for RhB and phenol degradation. Particularly, the as-prepared g-C$_3$N$_4$/Nb$_2$O$_5$ heterojunction exhibited higher photocatalytic activities towards the photodegradation of RhB and phenol under visible irradiation, compared to the pure g-C$_3$N$_4$ and Nb$_2$O$_5$ phases. The low bandgap energy (2.84 eV) as well as the synergistic effect between Nb$_2$O$_5$ NFs and g-C$_3$N$_4$ in the g-C$_3$N$_4$/Nb$_2$O$_5$ heterojunction enhanced the photocatalytic activity, which were beneficial to a rapid photoinduced charge separation in the electron transfer process and a slow charge recombination. In addition, both superoxide radical anion ($\cdot$O$_2^-$) and hole (h$^+$) were the major oxidative species for RhB and phenol degradation over the g-C$_3$N$_4$/Nb$_2$O$_5$ heterojunction photocatalyst. This work may provide a promising future of applying photocatalyst to solving dye pollutant problems and solar energy conversion.

References

1. Tkaczyk, A., Mitrowska, K. & Posyniak, A. Synthetic organic dyes as contaminants of the aquatic environment and their implications for ecosystems: A review. *Sci. Total Environ.* **717**, 137222 (2020).
2. Abdelsamad, A. M. A., Gad-Allah, T. A., Mahmoud, F. A. & Badawy, M. I. Enhanced photocatalytic degradation of textile waste-water using Ag/ZnO thin films. *J. Water Process Eng.* **25**, 88–95 (2018).
3. Zhou, J., Ding, J., Wan, H. & Guan, G. Boosting photocatalytic degradation of antibiotic wastewater by synergy effect of heterojunction and phosphorus doping. *J. Colloid Interf. Sci.* **582**, 961–968 (2021).
4. Yu, Y., Huang, Y., Yu, Y., Shi, Y. & Zhang, B. Design of continuous built-in band bending in self-supported CdS nanorod-based hierarchical architecture for efficient photoelectrochemical hydrogen production. *Nano Energy* **43**, 236–243 (2018).
5. Mendex-Medrano, M. G. *et al.* Surface modification of TiO$_2$ with Ag nanoparticle and CuO nanoclusters for application in photocatalysis. *J. Phys. Chem. C* **120**, 5143–5154 (2016).
6. Ani, I. J., Akpan, U. G., Olutoye, M. A. & Hameed, B. H. Photocatalytic degradation of pollutants in petroleum refinery wastewater by TiO$_2$- and ZnO-based photocatalysts: Recent development. *J. Clean. Prod.* **205**, 930–954 (2018).
7. Fu, S. *et al.* Design of TiO$_2$ nanocrystals with enhanced sunlight photocatalytic activity by exploring calcining conditions. *Ceram. Int.* **46**, 21268–21274 (2020).
8. Chakrabarti, S. & Dutta, B. K. Photocatalytic degradation of model textile dyes in wastewater using ZnO as semiconductor catalyst. *J. Hazard. Mater.* **112**, 269–278 (2004).
9. Park, S. J. *et al.* Visible-light photocatalysis by carbonnano-onion-functionalized ZnO tetrapods: Degradation of 2,4-dinitrophenol and a plant-model-based ecological assessment. *NPG Asia Mater.* **11**, 8 (2019).
10. Falk, G. *et al.* Colloidal sol-gel synthesis and photocatalytic activity of nanoparticulate Nb$_2$O$_5$ sols. *J. Am. Ceram. Soc.* **99**, 1968–1973 (2016).
11. Aslam, M. *et al.* The effect of sunlight induced surface defects on the photocatalytic activity of nanosized CeO$_2$ for the degradation of phenol and its derivatives. *Appl. Catal. B-Environ.* **180**, 391–402 (2016).
12. Li, Y., Wang, J., Yao, H., Dang, L. & Li, Z. Efficient decomposition of organic compounds and reaction mechanism with BiOI photocatalyst under visible light irradiation. *J. Mol. Catal. A-Chem.* **334**, 116–122 (2011).
13. Das, G. R., Bhatnagar, A., Yli-Pirila, P., Tripathi, K. M. & Kim, T. Sustainable nitrogen-doped functionalized graphene nanosheets for visible-light-induced photocatalytic water splitting. *Chem. Commun.* **56**, 6953–6956 (2020).
14. Kaushik, J. *et al.* Bio-mass derived functionalized graphene aerogel: A sustainable approach for the removal of multiple organic dyes and their mixtures. *New J. Chem.* **45**, 9073–9083 (2021).
15. Shi, W. *et al.* pH-controlled mechanism of photocatalytic RhB degradation over g-C$_3$N$_4$ under sunlight irradiation. *Photochem. Photobiol. Sci.* **20**, 303–313 (2021).
16. Andradea, F. V. *et al.* A new material consisting of TiO$_2$ supported on Nb$_2$O$_5$ as photocatalyst for the degradation of organic contaminants in aqueous medium. *J. Environ. Chem. Eng.* **2**, 2352–2358 (2014).

17. Li, B. *et al.* Photocatalytic selective hydroxylation of phenol to dihydroxybenzene by BiOI/TiO$_2$ p–n heterojunction photocatalysts for enhanced photocatalytic activity. *Appl. Surf. Sci.* **439**, 1047–1056 (2018).
18. Azami, M. S. *et al.* Formation of an amorphous carbon nitride/titania composite for photocatalytic degradation of RR4 dye. *J. Water Process Eng.* **35**, 101209 (2020).
19. Chin, Y., Sin, J. & Lam, S. A facile route for fabrication of hierarchical porous Nb$_2$O$_5$/ZnO composites with enhanced photocatalytic degradation of palm oil mill effluent. *Mater. Lett.* **216**, 8–11 (2018).
20. Ferraz, N. P. *et al.* CeO$_2$-Nb$_2$O$_5$ photocatalysts for degradation of organic pollutants in water. *Rare Met.* **39**, 230–240 (2020).
21. Xue, J., Wang, R., Zhang, Z. & Qiu, S. Facile preparation of C, N co-modified Nb$_2$O$_5$ nanoneedles with enhanced visible light photocatalytic activity. *Dalton T.* **45**, 16519–16525 (2016).
22. Kulkarni, A. K. *et al.* Nanostructured N-doped orthorhombic Nb$_2$O$_5$ as an efficient stable photocatalyst for hydrogen generation under visible light. *Dalton T.* **46**, 14859–14868 (2017).
23. Furukawa, S., Tamura, A., Shishido, T., Teramura, K. & Tanaka, T. Solvent-free aerobic alcohol oxidation using Cu/Nb$_2$O$_5$: Green and highly selective photocatalytic system. *Appl. Catal. B-Environ.* **110**, 216–220 (2011).
24. Lin, H., Yang, H. & Wang, W. Synthesis of mesoporous Nb$_2$O$_5$ photocatalysts with Pt, Au, Cu and NiO cocatalyst for water splitting. *Catal. Today* **174**, 106–113 (2011).
25. Bai, J., Xue, J., Wang, R., Zhang, Z. & Qiu, S. Synthesis of novel Au@Void@Nb$_2$O$_5$ core-shell nanocomposites with enhanced photocatalytic activity. *Dalton T.* **47**, 3400–3407 (2018).
26. Ahmad, Y. H., Eid, K., Mahmoud, K. A. & Al-Qaradawi, S. Y. Controlled design of PtPd nanodendrite ornamented niobium oxynitride nanosheets for solar-driven water splitting. *New J. Chem.* **42**, 14239–14245 (2018).
27. Ferrari-Lima, A. M., Marques, R. G., Gimenes, M. L. & Fernandes-Machado, N. R. C. Synthesis, characterisation and photocatalytic activity of N-doped TiO$_2$-Nb$_2$O$_5$ mixed oxides. *Catal. Today* **254**, 119–128 (2015).
28. Hashemzadeh, F., Gaffarinejad, A. & Rahimi, R. Porous p-NiO/n-Nb$_2$O$_5$ nanocomposites prepared by an EISA route with enhanced photocatalytic activity in simultaneous Cr(VI) reduction and methyl orange decolorization under visible light irradiation. *J. Hazard. Mater.* **286**, 64–74 (2015).
29. Marques, R. G., Ferrari-Lima, A. M., Slusarski-Santana, V. & Fernandes-Machado, N. R. C. Ag$_2$O and Fe$_2$O$_3$ modified oxides on the photocatalytic treatment of pulp and paper wastewater. *J. Environ. Manage.* **195**, 242–248 (2017).
30. Qi, S., Fei, L., Zuo, R., Wang, Y. & Wu, Y. Graphene nanocluster decorated niobium oxide nanofibers for visible light photocatalytic applications. *J. Mater. Chem. A* **2**, 8190–8195 (2014).
31. Wang, Y., Kong, X., Jiang, M., Zhang, F. & Lei, X. A Z-scheme ZnIn$_2$S$_4$/Nb$_2$O$_5$ nanocomposite: Constructed and used as an efficient bifunctional photocatalyst for H$_2$ evolution and oxidation of 5-hydroxymethylfurfural. *Inorg. Chem. Front.* **7**, 437–446 (2020).
32. Talapaneni, S. N. *et al.* Controlled synthesis of three dimensional mesoporous C$_3$N$_4$ with ordered porous structure for room temperature Suzuki coupling reaction. *Mol. Catal.* **477**, 110548 (2019).
33. Zhu, W., Song, H. & Lv, Y. Triazine-based graphitic carbon nitride: Controllable synthesis and enhanced cataluminescent sensing for formic acid. *Anal. Bioanal. Chem.* **410**, 7499–7509 (2018).
34. Erdogan, D. A. *et al.* Photocatalytic activity of mesoporous graphitic carbon nitride (mpg-C$_3$N$_4$) towards organic chromophores under UV and VIS light illumination. *Top. Catal.* **59**, 1305–1318 (2016).
35. Tang, Q., Meng, X., Wang, Z., Zhou, J. & Tang, H. One-step electrospinning synthesis of TiO$_2$/g-C$_3$N$_4$ nanofibers with enhanced photocatalytic properties. *Appl. Surf. Sci.* **430**, 253–262 (2018).
36. Qiao, Q. *et al.* Facile in situ construction of mediatorfree direct Z-scheme g-C$_3$N$_4$/CeO$_2$ heterojunctions with highly efficient photocatalytic activity. *J. Phys. D Appl. Phys.* **51**, 275302 (2018).
37. Wang, Y., Sun, J., Li, J. & Zhao, X. Electrospinning preparation of nanostructured g-C$_3$N$_4$/BiVO$_4$ composite films with an enhanced photoelectrochemical performance. *Langmuir* **33**, 4694–4701 (2017).
38. Carvalho, K. T. G., Nogueira, A. E., Lopes, O. F., Byzynski, G. & Ribeiro, C. Synthesis of g-C$_3$N$_4$/Nb$_2$O$_5$ heterostructures and their application in the removal of organic pollutants under visible and ultraviolet irradiation. *Ceram. Int.* **43**, 3521–3530 (2017).
39. Da Silva, G. T. S. T., Carvalho, K. T. G., Lopes, O. F. & Ribeiro, C. g-C$_3$N$_4$/Nb$_2$O$_5$ heterostructures tailored by sonochemical synthesis: Enhanced photocatalytic performance in oxidation of emerging pollutants driven by visible radiation. *Appl. Catal. B-Environ.* **216**, 70–79 (2017).
40. Hong, Y. *et al.* Efficient and stable Nb$_2$O$_5$ modified g-C$_3$N$_4$ photocatalyst for removal of antibiotic pollutant. *Chem. Eng. J.* **299**, 74–84 (2016).
41. Chang, G. *et al.* Self-constructed side-by-side nanofiber photocatalyst via opposite charged electrospinning and its photocatalytic degradation of rhodamine B. *New J. Chem.* **43**, 15405–15412 (2019).
42. Ma, G. *et al.* Constructing novel WO$_3$/Fe(III) nanofibers photocatalysts with enhanced visible-light-driven photocatalytic activity via interfacial charge transfer effect. *Mater. Today Energy* **3**, 45–52 (2017).
43. Ponnuvelu, D. V., Abdulla, S. & Pullithadathil, B. Novel electro-spun nanograined ZnO/Au heterojunction nanofibers and their ultrasensitive NO$_2$ gas sensing properties. *ChemistrySelect* **3**, 7156–7163 (2018).
44. Viet, A., Reddy, M. V., Jose, R., Chowdari, B. V. R. & Ramakrishna, S. Nanostructured Nb$_2$O$_5$ polymorphs by electrospinning for rechargeable lithium batteries. *J. Phys. Chem. C* **114**, 664–671 (2010).
45. Wang, K., Zhang, Y., Liu, L., Lu, N. & Zhang, Z. BiOBr nanosheets-decorated TiO$_2$ nanofibers as hierarchical p-n heterojunctions photocatalysts for pollutant degradation. *J. Mater. Sci.* **54**, 8426–8435 (2019).
46. Lu, M. *et al.* p-MoO$_3$ nanostructures/n-TiO$_2$ nanofiber heterojunctions: Controlled fabrication and enhanced photocatalytic properties. *ACS Appl. Mater. Interfaces* **6**, 9004–9012 (2014).
47. Zhang, Z. *et al.* Electrospun nanofibers of p-type NiO/n-type ZnO heterojunctions with enhanced photocatalytic activity. *ACS Appl. Mater. Interfaces* **2**, 2915–2923 (2010).
48. Yue, Z. *et al.* A novel heterogeneous hybrid by incorporation of Nb$_2$O$_5$ microspheres and reduced graphene oxide for photocatalytic H$_2$ evolution under visible light irradiation. *RSC Adv.* **5**, 47117–47124 (2015).
49. Huang, Z. *et al.* Effect of contact interface between TiO$_2$ and g-C$_3$N$_4$ on the photoreactivity of g-C$_3$N$_4$/TiO$_2$ photocatalyst: (001) vs (101) facets of TiO$_2$. *Appl. Catal. B-Environ.* **164**, 420–427 (2015).
50. Liang, Q. *et al.* Macroscopic 3D porous graphitic carbon nitride monolith for enhanced photocatalytic hydrogen evolution. *Adv. Mater.* **27**, 4634–4639 (2015).
51. Adhikari, S. P., Awasthi, G. P., Kim, H. J., Park, C. H. & Kim, C. S. Electrospinning directly synthesized porous TiO$_2$ nanofibers modified by graphitic carbon nitride sheets for enhanced photocatalytic degradation activity under solar light irradiation. *Langmuir* **32**, 6163–6175 (2016).
52. Li, K. *et al.* In-situ-reduced synthesis of Ti^{3+} self-Doped TiO$_2$/g-C$_3$N$_4$ heterojunctions with high photocatalytic performance under LED light irradiation. *ACS Appl. Mater. Interfaces* **7**, 9023–9030 (2015).
53. Hu, L., Yan, J., Wang, C., Chai, B. & Li, J. Direct electrospinning method for the construction of Z-scheme TiO$_2$/g-C$_3$N$_4$/RGO ternary heterojunction photocatalysts with remarkably ameliorated photocatalytic performance. *Chin. J. Catal.* **40**, 458–469 (2019).
54. Cao, D. *et al.* Lactic acid production from glucose over a novel Nb$_2$O$_5$ nanorod catalyst. *Catal. Lett.* **147**, 926–933 (2017).
55. He, J. *et al.* Hydrothermal growth and optical properties of Nb$_2$O$_5$ nanorod arrays. *J. Mater. Chem. C* **2**, 8185–8190 (2014).
56. Li, Y., Wu, X., Li, J., Wang, K. & Zhang, G. Z-scheme g-C$_3$N$_4$@C$_x$WO$_3$ heterostructure as smart window coating for UV isolating, Vis penetrating, NIR shielding and full spectrum photocatalytic decomposing VOCs. *Appl. Catal. B-Environ.* **229**, 218–226 (2018).

57. Lou, L. *et al.* Facile fabrication of interconnected-mesoporous T-Nb$_2$O$_5$ nanofibers as anodes for lithium-ion batteries. *Sci. China Mater.* **62**, 465–473 (2019).
58. Shekardasht, M. B., Givianrad, M. H., Gharbani, P., Mirjafary, Z. & Mehrizad, A. Preparation of a novel Z-scheme g-C$_3$N$_4$/RGO/Bi$_2$Fe$_4$O$_9$ nanophotocatalyst for degradation of Congo Red dye under visible light. *Diam. Relat. Mater.* **109**, 108008 (2020).
59. Liu, H. *et al.* One-step synthesis heterostructured g-C$_3$N$_4$/TiO$_2$ composite for rapid degradation of pollutants in utilizing visible light. *Nanomaterials* **8**, 842 (2018).
60. Huang, H., Zhou, J., Zhou, J. & Zhu, M. Structure-retentive synthesis of a highly ordered mesoporous Nb$_2$O$_5$/N-doped graphene nanocomposite with superior interfacial contacts and improved visible-light photocatalysis. *Catal. Sci. Technol.* **9**, 3373–3379 (2019).
61. Cheong, J. Y. *et al.* Mesoporous orthorhombic Nb$_2$O$_5$ nanofibers as pseudocapacitive electrodes with ultra-stable Li storage characteristics. *J. Power Sources* **360**, 434–442 (2017).
62. Zang, Y., Li, L., Xu, Y., Zuo, Y. & Li, G. Hybridization of brookite TiO$_2$ with g-C$_3$N$_4$: A visible-light-driven photocatalyst for As^{3+} oxidation, MO degradation and water splitting for hydrogen evolution. *J. Mater. Chem. A* **2**, 15774–15780 (2014).
63. Wang, S., Guan, B. Y., Wang, X. & Lou, X. W. D. Formation of hierarchical Co$_9$S$_8$@ZnIn$_2$S$_4$ heterostructured cages as an efficient photocatalyst for hydrogen evolution. *J. Am. Chem. Soc.* **140**, 15145–15148 (2018).
64. Ghugal, S. G., Umare, S. S. & Sasikala, R. Mineralization of anionic dyes over visible light responsive Cd(x)Zn(y)S-Nb$_2$O$_5$ heterostructured photocatalysts. *RSC Adv.* **6**, 64047–64055 (2016).
65. Wang, M. *et al.* Enhancement in the photocatalytic activity of TiO$_2$ nanofibers hybridized with g-C$_3$N$_4$ via electrospinning. *Solid State Sci.* **55**, 1–7 (2016).
66. Yan, J., Wu, G., Guan, N. & Li, L. Nb$_2$O$_5$/TiO$_2$ heterojunctions: Synthesis strategy and photocatalytic activity. *Appl. Catal. B-Environ.* **152–153**, 280–288 (2014).
67. Zhou, X. *et al.* A carbon nitride/TiO$_2$ nanotube array heterojunction visible-light photocatalyst: Synthesis, characterization, and photoelectrochemical properties. *J. Mater. Chem.* **22**, 17900–17905 (2012).

Acknowledgements

Author contributions

L.W. prepared photocatalysts and wrote the main manuscript text. Y.L. designed catalyst and measured the chemical structure of catalyst. P.H. performed manuscript revision and editing.

Competing interests

The authors declare no competing interests.

Additional information

Supplementary Information The online version contains supplementary material available at https://doi.org/10.1038/s41598-021-02161-x.

Correspondence and requests for materials should be addressed to P.H.

Reprints and permissions information is available at www.nature.com/reprints.

Publisher's note Springer Nature remains neutral with regard to jurisdictional claims in published maps and institutional affiliations.